Materials Today Bio 32 (2025) 101777

Contents lists available at ScienceDirect

Materials Today Bio

journal homepage: www.journals.elsevier.com/materials-today-bio

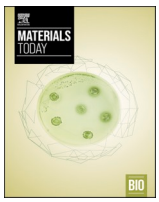

A microenvironment responsive nanoparticle regulating osteoclast fate to promote bone repair in osteomyelitis

Huan Zeng [a,b], Dize Li [a], Qingqing He [a], Xinhui Zheng [a], Xu Chen [a], Guangyu Jian [a], Hongmei Zhang [a,b,**], Tao Chen [a,*]

[a] Stomatological Hospital of Chongqing Medical University, Chongqing Key Laboratory of Oral Diseases and Biomedical Sciences, Chongqing Municipal Key Laboratory of Oral Biomedical Engineering of Higher Education, Chongqing, 401147, China
[b] Department of Pediatric Dentistry, The Affiliated Hospital of Stomatology of Chongqing Medical University, Chongqing, 401147, China

ARTICLE INFO

Keywords:
Inflammatory microenvironment
Modified nanoparticles
Metal-phenolic-network
Osteomyelitis
Osteoclast
pH-responsive

ABSTRACT

Osteomyelitis exhibits bone defects in an inflammatory and acid microenvironment. As a crucial factor in this inflammation responses, the macrophage-osteoclast axis is absolutely the core to regulate. The research explored a shell-core structured biomaterial, consisting of a gelatin nanoparticle (GNP) platform loaded with bone morphogenetic protein 9 (BMP9) and coated with a metal phenolic network (TA-Ce), which exhibited adaptive sensitivity to pH values. Extracellularly, it rapidly responded to lower pH, achieving specific release in an inflammatory microenvironment. Intracellularly, it impacted the formation, function, and differentiation of osteoclasts through the macrophage-osteoclast axis, thereby promoting bone defect repair. *In vivo* and *in vitro* studies showed GNPs-BMP9@TA-Ce regulated osteoclasts to optimize osteomyelitis treatment strategies, highlighting the potential of modified nanobiomaterials for clinical application.

1. Introduction

Osteomyelitis (OM) is an inflammatory process accompanied by bone destruction, caused by an infecting microorganism. These infections frequently manifest in the cortex, marrow, periosteum and the surrounding soft tissue [1]. OM is also associated with trauma, surgery, soft tissue spread, or periprosthetic implants. Current clinical treatment for chronic OM includes radical surgical debridement of the necrotic and infected tissues, along with prolonged courses of antibiotics [2,3]. Despite these measures, many patients experience prolonged bone recovery or develop comorbidities. Sometimes, bone grafting surgeries are adopted to confront the bone loss. OM presents a significant clinical challenge, associated with compromised quality of life, extensive morbidity, and even hospitalization [2].

Staphylococcus aureus (S. aureus) and its products can potently stimulate resorptive bone loss in OM, with direct actions (e.g., producing acid and proteases) leading to bone tissue destruction, alongside exacerbated leukocyte survival pathways [1,4,5]. They also directly increase osteoclasts formation and activity [6]. Bone destruction predominantly results from an uncoupling of osteoclasts and osteoblasts activities. Bone healing involves complex physiological processes initiated by the early regulation of inflammation [7]. In the inflammatory microenvironment, diversified immune cells are activated and release inflammatory factors including TNF-α, COX-2, Th17, IL-1, IL-3, etc. These factors regulate the osteoclast Rankl-Rank-OPG signaling pathway, triggering its differentiation and maturation. The acid environment caused by early bacterial infection promotes inflammatory polarization of macrophages. Meanwhile, a process driven by cytokines from activated cytotoxic T cells may prolong the presence of M1 macrophages, possibly by delaying their differentiation into more M2 macrophages [8–10]. A persistent, uncontrolled inflammatory environment further abnormally activates osteoclasts, leading to pronounced bone destruction. Additionally, more inflammatory mediators concomitantly depress OPG expression in osteoblasts and S. aureus similarly inhibits osteoblast production of RANKL decoy receptor [11]. These provide multifaceted mechanism of bone resorption at lesion sites. Notably, there is a close connection between OM biological events and osteoclasts. To match multiple levels of biological events, repair complex inflammatory microenvironments and promote bone healing, an integrated nanoplatform with multifunctionality and intelligent drug delivery capabilities is required.

* Corresponding author. The Affiliated Hospital of Stomatology of Chongqing Medical University, Songshi North Road, Yubei District, Chongqing, China.
** Corresponding author. The Affiliated Hospital of Stomatology of Chongqing Medical University, Songshi North Road, Yubei District, Chongqing, China.
E-mail addresses: hmzhang@hospital.cqmu.edu.cn (H. Zhang), chentao1985@hospital.cqmu.edu.cn (T. Chen).

https://doi.org/10.1016/j.mtbio.2025.101777
Received 13 January 2025; Received in revised form 30 March 2025; Accepted 16 April 2025
Available online 17 April 2025

Promoting bone repair in the lesion area and antibiotics treatment systemically, may be a novel approach to relieve OM. Substantial potential exists for developing tissue-engineered constructs as novel therapeutic options in clinics [12]. The properties of certain nanomaterials, such as realizing in situ cell therapy, pH responsiveness, collectively serve as the rationales to design a sustained-release bioresponsive drug delivery materials system [13–16].

The appropriate pH value of microenvironments is crucial for the physiological function and health. It may be affected by various factors, such as the accumulation of local metabolic products and inflammatory responses, leading to pH fluctuations. Deviations from the normal bone tissue pH of 7.2–7.4, which represents the homeostation, have been linked to various pathological conditions, including local and systemic inflammatory disorders [17,18]. Mature osteoclasts secrete organic acid, maintaining a local acid microenvironment at the inflammatory site, further lowering the pH. Numerous evidences indicate that the inflammatory bone destruction is attributed to an increase in the number of bone-resorbing osteoclasts. However, anti-resorptive therapy alone failed to prevent bone loss in an inflammatory condition. Bone resorption is a multi-step process involving precursor cell proliferation, differentiation into osteoclasts (osteoclastogenesis), and degradation of organic/inorganic structures by mature resorptive cells [19,20]. Therefore, regulating osteoclasts efficiently, combined with systemic anti-inflammatory treatment, could be a crucial strategy for drug development aimed at preventing inflammatory bone destruction.

TA and Cerium (IV) sulfate solution can form a flexible structure when vigorously shaken under mild conditions, through the classic Metal-Phenolic-Network (MPN) [21–23]. TA is a plant polyphenol containing five catechol groups and five galloyl groups, and it is a strong chelator for metal ions. During the reaction process, pH value is a key factor affecting the stability of MPN. Under neutral or weakly basic conditions, the catechol groups deprotonate, ensuring the formation of the TA-Ce coordination network. Conversely, TA-Ce rapidly degrades under acid conditions. In our early relevant studies [24–26], we have used TA and Ce to form an adaptable “chain armor” for substrate surfaces, aiming to regulate the pathological microenvironment in a responsive manner and ensure favorable osteointegration of the implant and host bone. Accordingly, we synthesized a gelatin nanoparticle (GNP) coated with a TA-Ce coordination network. Gelatin, a derivative of natural protein hydrogels abundant in animal skin and bone, has been widely used for biomedical applications such as osteoarthritis treatment [27]. Superior characteristics of gelatin include beneficial biological properties comparable to collagen, ease of processing into microspheres, gentle gelling behavior, controllable degradation characteristics by tailoring crosslinking conditions, and abundant presence of functional groups that allow for further functionalization and modification via chemical derivatization [27–31]. The reversible non-covalent interactions (electrostatic interactions) between gelatin nanoparticles enable the bottom-up assembly of gelatin particles into the continuous particulate network. Bone morphogenetic protein 9 (BMP9) has been reported as one of the most potent BMPs to induce bone remodeling [32–35] and can be used for bone tissue engineering when combined with some special biomaterials. We hypothesized that the modified GNPs loaded with BMP9 could achieve sustained release, responsing to the inflammatory microenvironment with a pH of approximately 5.5–6.5 [36]. When infected with S. aureus in an OM rat model, they are capable of bone repair. Our TA-Ce coordination film leads to an adaptive drug release through an effective biological response to the inflammatory acidic microenvironment. Additionally, we found that BMP9 could impede the precursors fusion, reduce osteoclasts differentiation, and impact their bone resorption function. Collectively, the modified GNPs with BMP9 offered an effective response to the inflammatory microenvironment and provided a new strategy for bone repair in OM rats.

2. Materials and methods

2.1. Materials

Tannic acid (TA), Cerium (IV) sulfate, sodium hydroxide (NaOH), hydrochloric acid (HCL), gelatin nanoparticle powder, BSA, RhodaMine labeled BSA (BSA/RBITC), Murine sRank-Ligand (Rankl), Recombinant Macrophage Colony Stimulating Factor 1 (M-CSF), Lipopolysaccharide (LPS), Recombinant Mouse BMP9, phosphate buffered saline (PBS), RPMI-1640, FBS, DMEM, Crystal Violet Staining Solution, penicillin-streptomycin, Counting Kit-8, Tartrate-resistant acid phosphatase (TRAP) staining kit, Phallotoxin, transwell, DAPI, RNAiso Plus reagent and TB GreenTM Premix Ex *Taq*II, Rhodamine B (RhB), Lysotracker Green DND-26, Hoechst 33342, DAPI, anti-IL-1β, CY3 IgG, Triton X-100, paraformaldehyde (PFA). All reagents were used directly without further processing.

2.2. Preparation of GNPs@TA-Ce,GNPs-BMP9@TA-Ce and GNPs-BSA/RBITC@TA-Ce, GNPs-BSA@TA-Ce

We synthesized the GNPs@TA-Ce using an established protocol. Firstly, 40 mg GNPs were added to 40 mL sterile double distilled water (ddH_2O). Then, TA solution (200 μL, 24 mmol/L) and Cerium (IV) sulfate (1.2 mL, 24 mmol/L) were sequentially added. Every step was executed by vortexing for 10 s rapidly. Then, NaOH solution (120 μL, 1 M) was added to adjust the pH value above 8.0. Nanoparticles were gathered by washing and centrifugation for three times. After freeze-drying overnight, pure GNPs@TA-Ce were harvested finally.

GNPs@TA-Ce loaded with BMP9 (GNPs-BMP9@TA-Ce) were synthesized by first reacting BMP9 solution (1 mL, 400 ng/mL) with 1 mg GNPs powder in a tube at 4 °C overnight. After imbibition and swelling, this gelatin was mixed with 10 mL ddH_2O subsequently. Then, TA solution (50 μL, 24 mmol/L) and $Ce(SO4)_2$ (300 μL, 24 mmol/L) were sequentially added. Every step was executed by vortexing for 10 s rapidly. Then, NaOH solution (30 μL,1 M) was added to adjust the pH value above 8.0. Finally, the materials were washed for three times. After freeze-drying overnight, GNPs-BMP9@TA-Ce were harvested.

GNPs@TA-Ce loaded with BSA/RBITC (GNPs-BSA/RBITC@TA-Ce) were synthesized by first reacting 40 mL BSA/RBITC solution (1 mg/mL) with 40 mg GNPs powder at 4 °C overnight. After adequate imbibition and swelling, this gelatin was mixed with 10 mL ddwater. Then, 200 μL the TA solution (24 mmol/L) and 1.2 mL Cerium (IV) sulfate (24 mmol/L) were added sequentially. Every step was executed by rapidly vortexing for 10s. After that, 120 μL NaOH solution (1 M) was added to adjust the pH value above 8.0. Finally, the materials were washed for three times. After freeze-drying overnight overnight, GNPs-BSA/RBITC@TA-Ce were harvested. All the above operations should be protected from exposure to light.

GNPs@TA-Ce loaded with BSA (GNPs-BSA@TA-Ce) were synthesized by first reacting 40 mL BSA solution (1 mg/mL) with 40 mg GNPs powder at 4 °C overnight. After adequate imbibition and swelling, this gelatin was mixed with 10 mL ddwater. Then, 200 μL the TA solution (24 mmol/L) and 1.2 mL Cerium (IV) sulfate (24 mmol/L) were added sequentially. Every step was executed by rapidly vortexing for 10s. After that, 120 μL NaOH solution (1 M) was added to adjust the pH value above 8.0. Finally, the materials were washed for three times. After freeze-drying overnight overnight, GNPs-BSA@TA-Ce were harvested.

2.3. Characterizations

Field-emission scanning electron microscopy (FE-SEM) and transmission electron microscope (TEM) were used to analyze the surface morphology and elemental distribution of GNPs@TA-Ce. The ionic composition was detected by EDX mapping and valences were tested by XPS. Nanoparticles size were obtained by Dynamic light scattering (DLS). *Ray Diffractomer (XRD) was used to explore its structure.*

GNPs@TA-Ce and GNPs were dispersed in HPEPS (5 mM); Then the Zeta potential was measured using a Zetasize® Nano-S instrument. Raman spectrometer was used to detect chemical bond. *UV–Vis spectrophotometer was used to analyze absorbances.*

2.4. pH-responsive drug release

Cumulative drug release amounts of GNPs-BSA/RBITC@TA-Ce were measured using Cary 5000 UV–Vis spectrophotometer. First, a calibration curve was obtained by plotting the absorbance BSA/RBITC at 495 nm as a function of increasing concentration. GNPs-BSA/RBITC@TA-Ce were dispersed in buffers of different pH values 5.5 and 7.4 individually with cellulose ester dialysis membranes (MWCO 10kd). The samples need to be kept away from light with gentle shaking. Quantitative supernatants were withdrawn at periodic intervals, and equal amounts of buffer were added back to the main sample. The collected supernatants were analyzed using UV–Vis spectroscopy to calculate BSA/RBITC release with the previous calibration curve.

Cumulative drug release amounts of GNPs-BSA@TA-Ce were measured by UV–Vis spectrophotometer 2500. First, a calibration curve was obtained by plotting the absorbance BSA at 240 nm as a function of increasing concentration. GNPs-BSA@TA-Ce were dispersed in buffers of different pH values 5.5 and 7.4 individually with cellulose ester dialysis membranes (MWCO 10kd). Quantitative supernatants were withdrawn at periodic intervals, and equal amounts of buffer were added back to the main sample. The collected supernatants were analyzed using UV–Vis spectroscopy to calculate BSA release with the previous calibration curve.

GNPs@TA-Ce were dispersed in buffers of different pH values 5.5 and 7.4 individually to detect Ce release by ICP-OES.

2.5. In vitro degradation

Weigh out several 400 mg samples of the freeze-dried GNPs-BSA@TA-Ce powder.

Place each sample in 40 mL PBS (pH 7.4) at 37 °C for degradation. Record the dry

weight of the samples after freeze-drying at each time point, and then calculate the *in*

vitro degradation rate of the GNPs-BSA@TA-Ce.

2.6. Culture of S. aureus and RAW 264.7

S. aureus was cultured in Luria−Bertani medium, washed twice (0.9 % NaCl solution) and centrifugated (6000 rpm, 10 min) for further experiment use. RAW 264.7 were cultured in growth medium (1 % penicillin streptomycin, 10 % FBS, 89 % DMEM) at 37 °C, 5 % CO2.

2.7. Isolation and culture of BMDMs

Male mice aged 4–6 weeks were sacrificed with carbon dioxide, and their tibias were aseptically collected. The bone marrow was flushed out with basic medium (BM) [89 % 1640 medium, 10 % FBS, 1 % penicillin-streptomycin]. A 40 μm cell strainer was used to sieve the bone marrow suspension. Then it were lysed (with red cell lysis buffer) and centrifuged (500g, 5 min). The cell precipitate was then resuspended in complete medium(BM with 50 ng/mL M-CSF)and incubated at 37 °C and 5 % CO^2. Non-adherent cells were collected after 24 h for further culture. Two or three days later, the adherent cells (BMDMs) were ready for further experiment.

2.8. Induction of osteoclasts and different biomaterials treatment

BMDMs were incubated with a density of 2×10^5 cells/cm^2 onto 24-well and 48-well plates in osteoclastogenic medium (BM with 50 ng/mL RANKL and 50 ng/mL M-CSF). The medium was refreshed every two days. LPS (10 ng/mL) was introduced into osteoclastogenic medium after 24 h. Cultures in 24-well plates were subjected to qPCR. Cultures in 24-well plates with cell slides were subjected to cytoskeleton staining, immunofluorescence staining and subcellular localization of GNPs@TA-Ce in BMDMs. Cultures in 48-well plates were used for TRAP staining.

Materials of different groups (GNPs-BMP9 0.25 mg/mL, GNPs@TA-Ce 0.25 mg/mL, GNPs-BMP9@TA-Ce 0.25 mg/mL) were added into the osteoclastogenic medium for biological materials treatment in the qPCR, cytoskeleton staining, immunofluorescence staining experiments.

2.9. Phalloidin fluorescence staining

For detection of the cytoskeleton and cell morphology of osteoclasts, BMDMs were seeded at 1×10^5 cells/cm^2 on the surface of cell slides in 24-well plates with osteoclastogenic medium. After treatment with different materials for 72 h, cells were fixed with 4 % PFA, washed with PBS, and permeabilized with 0.2 % Triton X-100 in PBS. Samples were incubated with Alexa Fluor 488 phalloidin and counterstained with DAPI. Images were acquired in LSCM.

2.10. Immunofluorescence staining

After treatment with different materials for 24 h, cells were fixed with 4 % PFA, washed with PBS, and permeabilized with 0.1 % Triton X-100. Next, samples were incubated with IL-1β monoclonal antibody, followed by incubation with anti-IgM AF594 and DAPI. Images were captured by LSCM. The 3D surface plot was analyzed using ImageJ. A higher peak indicated more pronounced infiltration.

2.11. Subcellular localization of GNPs@TA-Ce in BMDMs

We synthesized RhB labeled GNPs@TA-Ce as follows: firstly, 40 mg GNPs were added to 40 mL ddH_2O. Then, TA solution (200 μL, 24 mmol/L) and RhB (200 μL, 0.4 mmol/L) and Cerium (IV) sulfate (1.2 mL, 24 mmol/L) were added. Every step was executed by vortexing for 10 s rapidly. Then, NaOH solution (120 μL, 1 M) was added to adjust the pH value above 8.0. Nanoparticles were gathered by washing and centrifugation for three times. RhB labeled GNPs@TA-Ce were harvested finally.

After treatment with LPS (10 ng/mL) for 6 h, BMDMs were added fresh medium (containing 10 μg/mL RhB labeled GNPs@TA-Ce) and incubated for 4 h and 24 h. Discard the medium, wash each well with PBS three times, add fresh medium with LysoTracker Green staining for 30 min at 37 °C. Discard the medium, wash each well with PBS three times, add Hoechst for 8 min at room temperature. Observe the subcellular localization of GNPs@TA-Ce in BMDMs by LSCM.

2.12. qPCR

BMDMs were incubated with osteoclastogenic medium and materials of different groups for 48 h. The transcription of osteoclasts-related genes were evaluated, including nuclear transcription factor of activated T cells c1 (NFATc1), DC-specific transmembrane protein associated with antigen processing (DC-SATMP), cathepsin K (CTSK), matrix metallopeptidase 9 (MMP9), and Tartrate-resistant acid phosphatase (TRAP). Quantitative RT reactions were performed by using iQ™ SYBR® Green Supermix and iQ™5 Multicolor Real-Time PCR Detection System according to the manufacturer's recommendations. The primers and GAPDH used as the internal control were as follows: NFATc1, forward 5′-TGTTCTTCCTCCCGATGTCT-3′ and reverse 5′-CCCGTTGCT TCCAGAAAATA-3'; DC-SATMP, forward 5′- TCCTCCATGAACAAA-CAGTTCCAA-3′ and reverse 5′ AGACGTGGTTTAGGAATGCAGCTC-3'; CTSK, forward 5′-CTGCTGGTA ACGGATCAGCTC CCCAGA-3′ and reverse 5′-CCAAGGAGCCAGAACCTTCGAAACT-3'; MMP9, forward 5′-TGGTGTGCCCTGGAACTCA-3′ and reverse 5′-GGAAAC TCA-CACGCCAGA AGA-3'; TRAP, forward 5′-

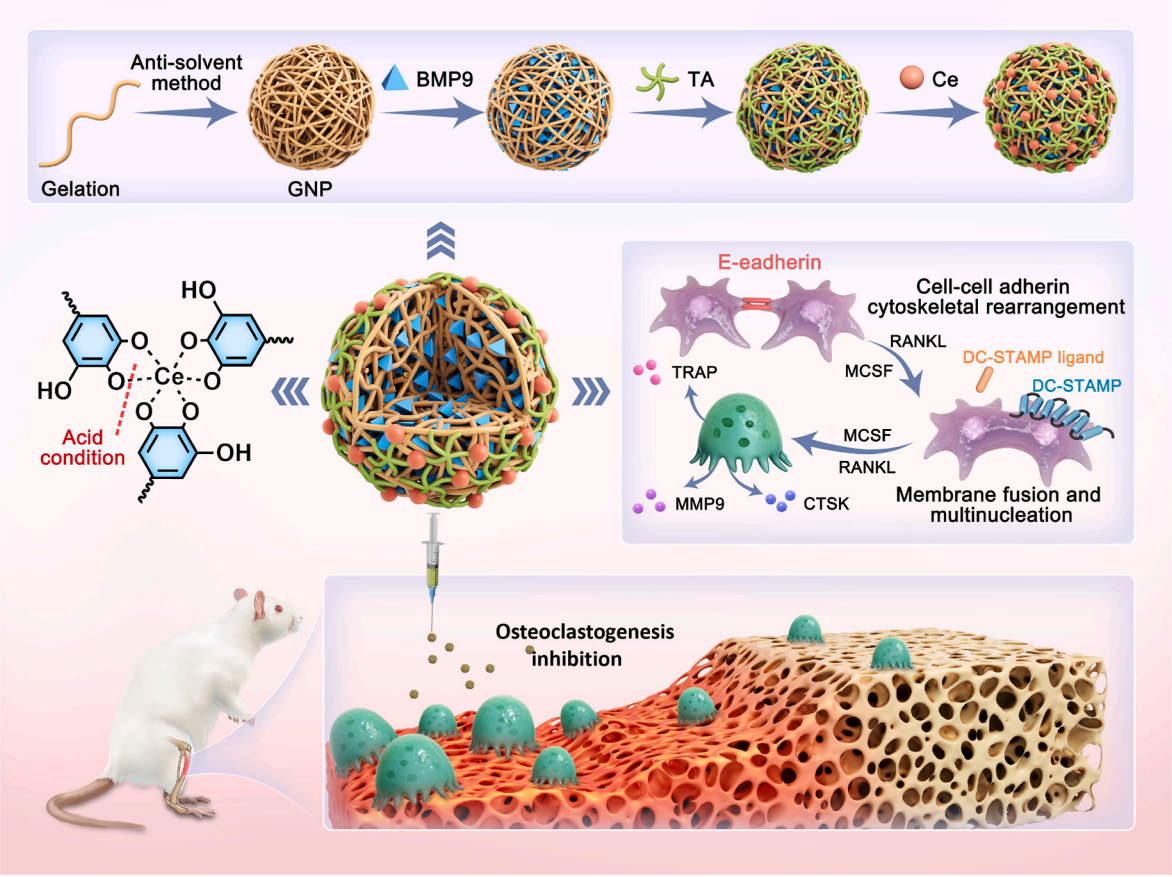

Scheme 1. The design of microenvironment responsive GNP-BMP9@TA-Ce and its mechanism of OM treatment by osteoclast regulation.

CTGGAGTGCACGATGCCAGCGACA-3 and reverse 5′-TCCGTGCTCGGCGATGGACCAGA-3'; GAPDH, forward 5′-AAA TGGTGAAGGTCGGTGTG-3′ and reverse 5′-TGAAGGGGTCGTTGATGG-3'.

2.13. Trap staining

After osteoclastogenic induction for 5 days with biomaterials treatment of different groups, cells were washed twice and fixed with 4 % PFA for 15 min, followed by permeabilization with 0.1 % Triton X-100 for 10 min. Fixed cells were stained using TRAP stain kit for 30 min in the darkat 37 °C, following the manufacturer's instructions. TRAP + multinuclear (nuclei >3) cells were counted(randomly select 6 fields of view at 100× magnification, repeating 3 times).

2.14. OM animal model with bacterial

All animal experiments were approved by the Animal Ethics Committee of Chongqing Medical University. All experiments followed the ARRIVE guidelines. Sprague−Dawley (SD) rats (250−320 g, male) were housed under Specific pathogen-free (SPF) conditions. For the construction of the OM animal model, a defect (1.5 mm × 1.5 mm) was created in the tibias. Rats were assigned to four groups to study the effects of OM repair as group 1 (control), group 2 (OM), group 3 (4-week GNPs-BMP9@TA-Ce treatment), group 4 (12-week GNPs-BMP9@TA-Ce treatment) randomly ($n \geq 3$). Apart from the control group, all others were injected with S. aureus bacterial suspension (1×10^6 CFU/mL) into the defects. Then the defects of treatment groups (4-week and 12-week GNPs-BMP9@TA-Ce treatment groups) were injected with 200 μL GNPs-BMP9@TA-Ce. Rats were euthanized with carbon dioxide at the time point of week 4 or week 12. Their tibias were harvested for further

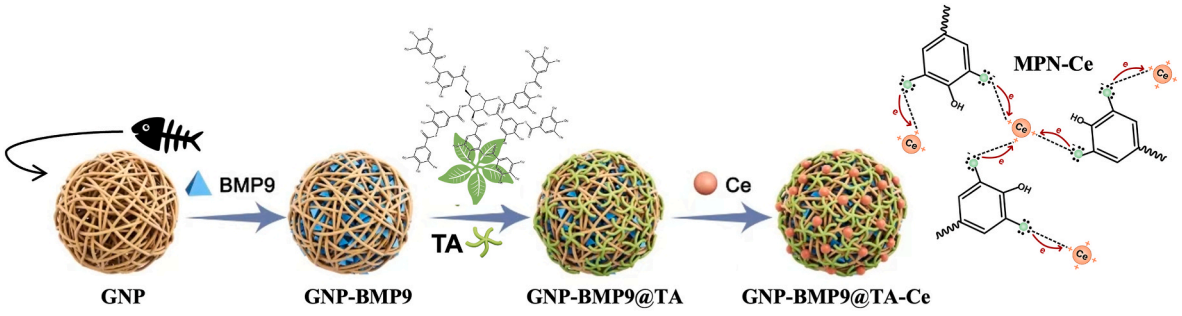

Fig. 1. Steps of GNP-BMP9@TA-Ce synthesis.

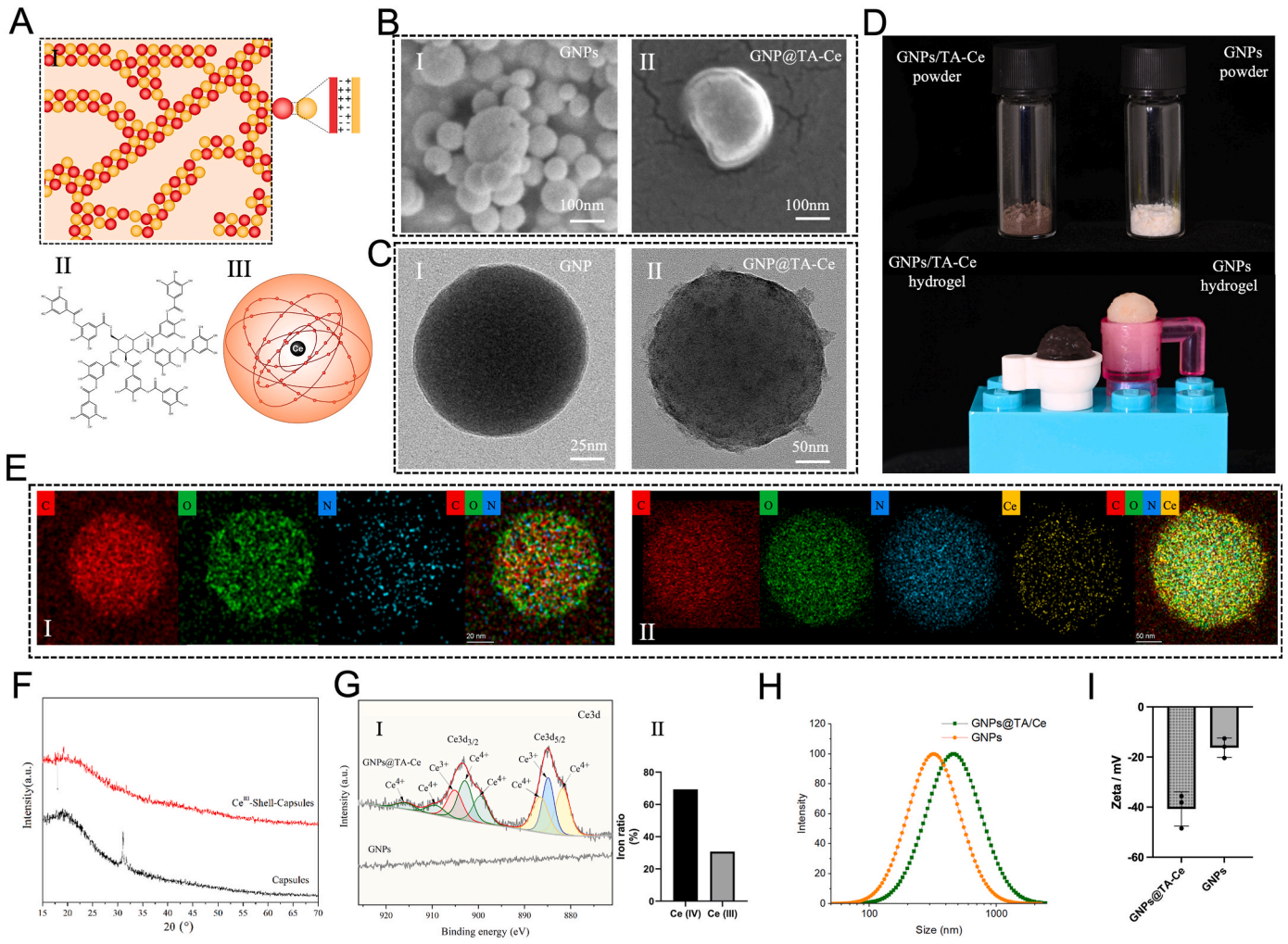

Fig. 2. Synthesis, structural properties and characterization of the GNPs-BMP9@TA-Ce
(A) the synthetic compents of GNPs@TA-Ce. I) Gelatin network formed by the crosslinking of positive and negative charges. II) Molecular structure of TA. III) The nucleus and surrounding electron arrangement of Cerium atom. **(B)** SEM images of GNP (I) and GNP@TA-Ce (II). Scale bar: 100 nm. **(C)** TEM images of GNP (I) and GNP@TA-Ce (II). Scale bar in image I: 25 nm. Scale bar in image II: 50 nm. **(D)** Photographs showing that the GNPs powder, GNPs@TA-Ce powder, and their hydrogel samples. **(E)** EDX mapping of GNP (I) and GNP@TA-Ce (II). Scale bar in image I: 20 nm. Scale bar in image II: 50 nm. **(F)** XRD patterns of GNPs and GNPs@TA-Ce. **(G)** I)High resolution XPS spectra of Ce 3d for GNPs@TA-Ce. II)Iron ratio of Ce (IV) and Ce (III) in GNPs@TA-Ce. **(H)** Particle size analysis of GNPs and GNPs@TA-Ce detected through DLS. **(I)** Zeta potential analysis of GNPs and GNPs@TA-Ce.

experiments.

2.15. Micro-CT test

Bone repair was detected by Micro-CT. The scanning parameters were set as follows: exposure time 3000 ms, resolution 6 μm, 70 kV, 112 μA. 3D images of the area of interest were reconstructed for further analysis using CT80 and Materialise Magics 24.0. Bone volume/tissue volume (BV/TV) and Tb.N were calculated for quantitative analysis.

2.16. Statistical analysis

SPSS 20.0 was used for data analysis. The comparison of quantitative data was conducted by one-way ANOVA. Post comparisons were presented by tukey's post hoc important difference test. P* <0.05 means statistically significant.

3. Results and discussion

3.1. Synthesis and characterization of GNPs@TA-Ce

Gelatin nanoparticles powder was provided by Huanova Biotech (Shenzhen, China) and prepared based on a previously reported two-step desolvation method. The synthesis and osteoclast regulation of GNPs-BMP9@TA-Ce responsive to inflammatory microenvironment was shown in Scheme 1. Procedures of GNPs-BMP9@TA-Ce synthesis is shown in Fig. 1. BMP9 was loaded into the GNPs through swelling and imbibition action. TA-Ce film was assembled by combining TA and Ce on the surface of GNPs, through the classic MPN system. The main synthetic components, including GNPs, Tannic Acid (TA), and $Ce(SO_4)_2$ were shown in Fig. 2A. Significantly, the multiple hydroxyl groups of TA provided abundant electrons for the active Ce (III) and Ce (IV), facilitating the formation of MNP-Ce.

Images detected by SEM compared between GNPs (Fig. 2BI) and GNPs@TA-Ce (Fig. 2BII) revealed the GNP@TA-Ce was shell-core structure with a flexible layer. TEM images comparing GNPs and GNPs@TA-Ce showed that TA-Ce uniformly coated the GNPs (Fig. 2CI), confirming the synthesis of GNPs@TA-Ce (Fig. 2CII). Photographs

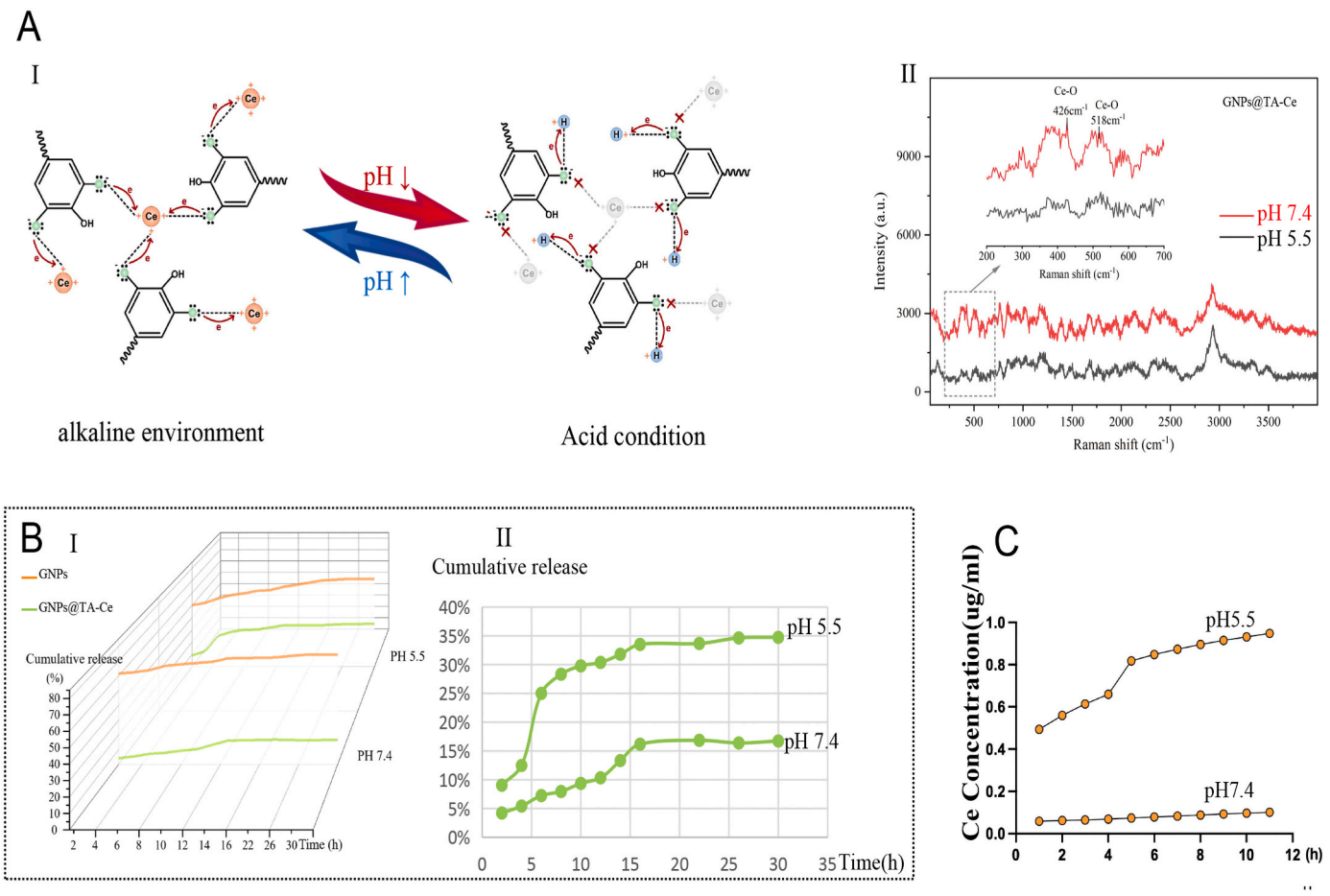

Fig. 3. Schematic images of pH-responsive TA-Ce and the response of GNPs@TA-Ce to the different microenvironment
(A) Chemical structures of TA-Ce in different pH environments. I) Schematic images of TA-Ce in different pH environments. II) Raman spectra image of GNPs@TA-Ce in pH 5.5 (black spectra) and pH 7.4 (red spectra). **(B)** the response of GNPs-BSA/RBITC@TA-Ce to the different pH values. I) the cumulative BSA/RBITC release of GNPs-BSA/RBITC and GNPs-BSA/RBITC@TA-Ce in pH 5.5 and 7.4. II) the cumulative BSA/RBITC release of GNPs-BSA/RBITC@TA-Ce in pH 5.5 and 7.4. **(C)** Ce Concentration released by GNPs@TA-Ce in pH 5.5 and 7.4. (For interpretation of the references to color in this figure legend, the reader is referred to the Web version of this article.)

showed two different forms of GNPs@TA-Ce (Fig. 2D). Similar to GNPs, freeze-dried GNPs@TA-Ce powder was easy to store, enabling large-scale production of biomaterials. Moreover, they can form hydrogels quickly through reaction with solutions. The favorable fluidity and deformability ensured local medication application, whether by injection or external use. EDX mapping demonstrated that C and Ce (contained within the TA-Ce) were further filmed on GNPs (Fig. 2EI), forming GNPs@TA-Ce (Fig. 2EII) with Ce well-dispersed in the film. Due to the assembly of TA, rich in benzene rings and hydroxyl groups, the content of C and O in GNPs@TA-Ce underwent significant changes (Fig. S1). The XRD pattern of GNPs@TA-Ce indicated their amorphous structure (Fig. 2F). XPS confirmed the successful modification of Ce ions on GNPs. The XPS spectra of Ce 3d in GNPs@TA-Ce was shown in Fig. 2GI. As shown in Fig. S2, the spectrum of Ce 3d revealed characteristic peaks at 881.75, 884.78, 886.51, 899.53, and 915.74eV attributed to Ce 3d 5/2 and Ce 3d 3/2 of Ce (IV); Peaks at 902.92, 905.11 and 909.24 eV were attributed to Ce 3d 5/2 and Ce 3d 3/2 of Ce (III). Ce (IV) to Ce (III) ratio was 2.26:1 (Fig. 2GII). Ce (IV), exhibiting high oxidase-like activity, was reduced to form Ce (III) with the electron-donating effect from TA in an alkaline environment, further confirming the formation of MPN-Ce. In general, the precise modification method enabled the film's suitability for multiple substrates. Compared to other substrates, GNPs possess distinctive properties, including low biotoxicity, surface and boundary effects, and small size effects [37,38]. Absolutely, GNPs@TA-Ce also exhibited good biocompatibility (Fig. S3). The ratio of particle surface area to volume increases as its diameter decreases significantly [39]. The high surface area of GNPs@TA-Ce is likely to result in different properties, compared to other objects coated with MPN films. Furthermore, DLS was used to demonstrate the different dimension of GNPs and GNPs@TA-Ce. Due to the TA-Ce film, average diameters of GNPs@TA-Ce were marginally larger (Fig. 2H). The difference in zeta potential further proved the successful film modification, as it showed in Fig. 2I.

3.2. *pH responsive release manner of GNPs@TA-Ce*

Compared with traditional modification, microenvironment-responsive delivery to tissue offers unprecedented strategy and reduces toxic side effects for precisely targeted treatment towards to the microenvironment [16]. The pH value of the inflammatory microenvironment is lower. Thus, we investigated the bio-decomposition behavior of GNPs@TA-Ce in different pH buffers between physiological conditions (pH 7.4) and OM environments (pH 5.5).

During the assembly process of TA-Ce (Fig. 3AI), the catechol and galloyl groups of TA provide active electrons, forming coordination bonds with Ce (III) and Ce (IV) to generate supramolecular network structures in an alkaline condition. Depending on different pH values, TA-Ce can form mono-complexes, bi-complexes, or tri-complexes. However, these coordination bonds are pH-dependent. When the pH is lowered to acid conditions, the competition between hydrogen ions and

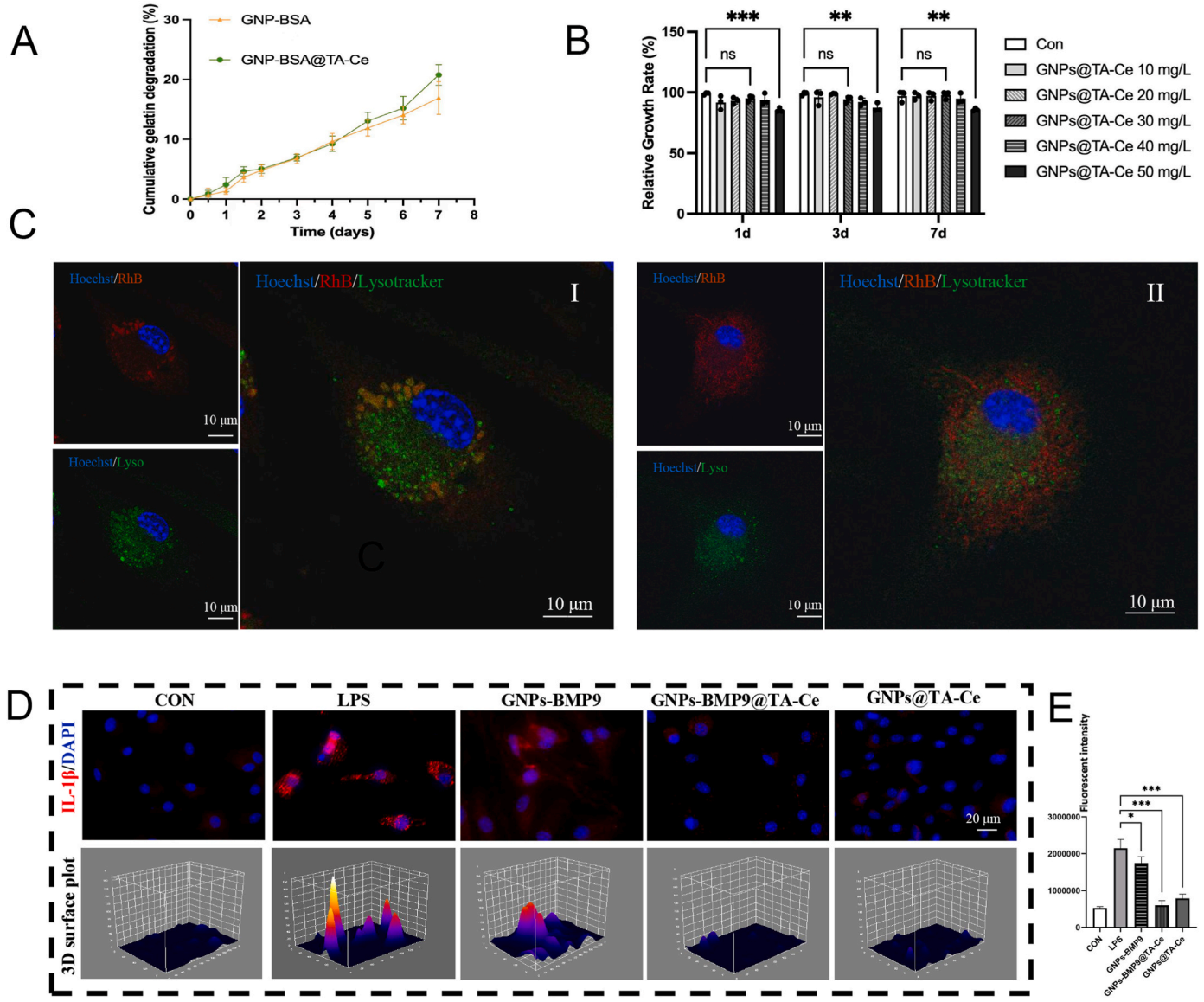

Fig. 4. Degradation, biosafety of GNPs-BMP9@TA-Ce and its effect on BMDMs
(A) The cucumlative degradation of GNPs-BSA and GNPs-BSA@TA-Ce in 7 days. **(B)** The *in vitro* cytotoxicity against BMDMs after co-culture with GNPs@TA-Ce for different time at different concentrations. *P < 0.05, **P < 0.01, ***P < 0.001. **(C)** LSCM images of BMDMs co-culture with 10 μg/mL RhB-labeled GNPs@TA-Ce at different time points. The GNPs@TA-Ce were stained red with RhB. The nuclei were stained blue with Hoechst. The lysosomes were stained green with Lysotracker. (I) Representative image of BMDMs co-cultured with GNPs@TA-Ce for 4 h scale bar: 10 μm. (II) Representative image of BMDMs co-cultured with GNPs@TA-Ce for 24 h scale bar: 10 μm. **(D)** Representative immunofluorescent images of the intracellular IL-1β in BMDMs co-cultured with different biomaterials for 24 h. Nuclei: blue. IL-1β: red. Scale bar: 20 μm. **(E)** Immunofluorescence quantitative analysis of the intracellular IL-1β in BMDMs co-cultured with different biomaterials for 24 h *P < 0.05, **P < 0.01, ***P < 0.001. (For interpretation of the references to color in this figure legend, the reader is referred to the Web version of this article.)

metal ions for chelation occurs, and some of the phenolic hydroxyl groups on the polyphenol molecules are protonated by hydrogen ions in the acid environment, causing the TA-Ce to become unstable or even disintegrate. Raman spectroscopy was employed to analyze the GNPs@TA-Ce obtained under different pH conditions. The characteristic peaks observed at 426 cm^{-1} and 518 cm^{-1} correspond to the Ce-O stretching vibration. Compared with pH 5.5, the higher intensity observed at pH 7.4 indicated enhanced formation of Ce-O bonds and greater participation of Ce in the chemical complexation within TA-Ce. We used BSA/RBITC as a model drug to simulate cumulative release experiments *in vitro*. GNPs loaded with BSA/RBITC (GNPs-BSA/RBITC) were used as the control group, while GNPs-BSA/RBITC@TA-Ce were used as the experimental group. The cumulative drug release was calculated by measuring the concentration of BSA/RBITC in solutions of different pH values through a concentration-release standard curve (Fig. S4A). We found GNPs were more prone to burst release in a physiological environment with pH 7.4; However, due to the protection of the TA-Ce film, GNPs@TA-Ce can release drugs more gently. In cases requiring higher drug stability, degradation resistance, or a gradual release pattern, core-shell or inner-outer architectures can protect the drug from the surrounding milieu, maximizing its *in vivo* delivery efficiency [40]. Moreover, in an acid condition with pH 5.5, GNPs@TA-Ce responded quickly to pH changes, releasing an adequate amount of drugs; Subsequently, its release calmed down, allowing for sustained drug release in the local lesion area, maintaining a long-term effective drug concentration (Fig. 3BI). More interestingly, when comparing the drug release activity of GNPs@TA-Ce in different microenvironments with different pH values, we discovered that once the low pH triggered, the "smart" GNPs@TA-Ce could respond sensitively to the acidic microenvironment. They released more drugs to rapidly relieve the

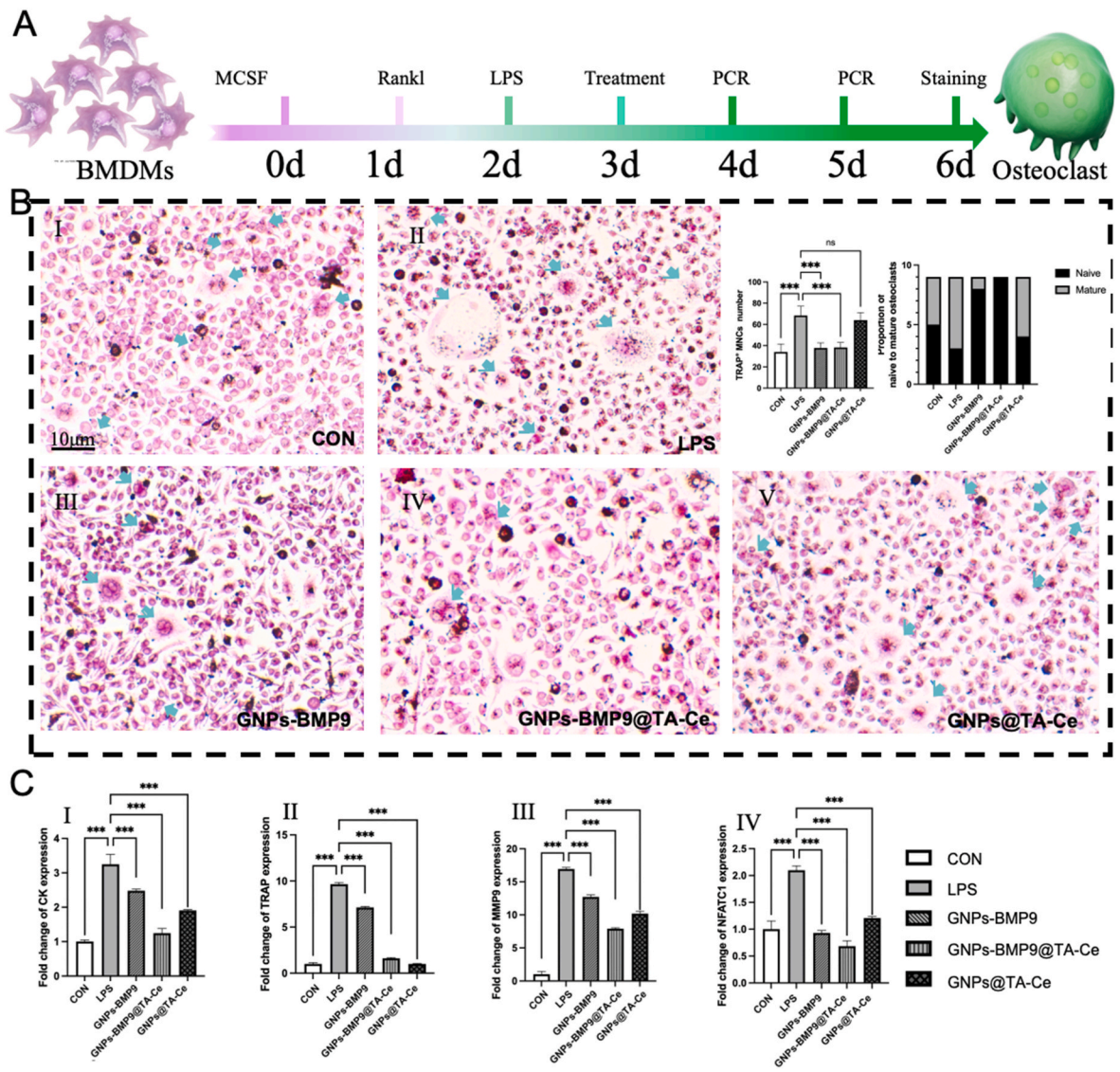

Fig. 5. Effect of GNPs-BMP9@TA-Ce on osteoclasts formation and function in LPS-induced inflammatory microenvironment
(A) Experimental timeline design for different biomaterials treating osteoclasts. **(B)** The Trap staining of control (I), LPS (II), GNPs-BMP9 (III), GNPs-BMP9@TA-Ce (IV), GNPs@TA-Ce (V) groups. Osteoclasts were marked with blue arrows. Quantitative analysis of the number of TRAP + MNCs. Scale bar: 10 μm. **(C)** the gene expression of functional biomakers (CTSK、TRAP、MMP9) of osteoclasts treated with different biomaterials. Data were presented as means ± SD ($n \geq 3$). ***$p < 0.001$, ns: no significance. (For interpretation of the references to color in this figure legend, the reader is referred to the Web version of this article.)

disease, then (after about 16 h) they resumed sustained release characteristics in the acidic microenvironment (Fig. 3BII). To reduce the interference of fluorescence, We further used BSA as a model drug to investigate the release behavior of GNPs@TA-Ce at pH 5.5 and pH 7.4. The experimental procedures were performed as previously described about BSA/RBITC release. The cumulative BSA release was calculated by measuring the concentration of BSA in solutions of different pH values through the concentration-release standard curve (Fig. S4BI). Consistent with prior findings, these results reaffirm the pH-responsive release characteristics of GNPs@TA-Ce as shown in Fig. S4BII. Based on the above conclusion, we used ICP to detect the Ce concentration to further study the release behavior of GNPs@TA-Ce in the acidic condition at the early stage. Interestingly, the Ce concentration remained low, indicating the stability of GNPs@TA-Ce under the physiological condition. This indicated GNPs@TA-Ce can carry targeted drugs. However, under the acidic condition with the pH of 5.5, the Ce concentration rapidly increased within 0–5 h, suggesting continuous and rapid decomposition of the "film" and a large amount of drug release simultaneously. The GNPs@TA-Ce made rapid and precise responses to the low pH value to achieve an effective drug concentration in a timely manner. After 5–10 h, the release began to level off, exerting a long-term effect on the local lesion. The ICP results were basically consistent with the cumulative release experiment.

Images (Fig. S5) by TEM showed that the spherical structure of GNP@TA-Ce was more significantly destroyed in an acidic microenvironment (pH 5.5), compared with those *in vitro* physiological conditions (pH 7.4). As TA-Ce failed under acidic conditions, swelling and imbibition effects were pronounced, leading to a larger volume. This demonstrated the degradation process of GNPs@TA-Ce and its pH-responsive capacity.

In general, GNPs@TA-Ce can depolymerize rapidly in a pH-responsive manner under inflammatory conditions. Then, GNPs@TA-Ce showed sustained release capabilities to implement long-term medication treatment smartly.

3.3. *Effect of GNPs-BMP9@TA-Ce on BMDMs*

To study the effect of GNPs-BMP9@TA-Ce on osteoclast precursors,

we co-cultured different groups of biomaterials (GNPs-BMP9, GNPs-BMP9@TA-Ce, GNPs@TA-Ce) with LPS-induced BMDMs. To ensure the sustained effect of biomaterials on BMDMs, we simulated the biodegradation *in vitro* for 7 days; we used BSA as the simulated drug and detected the degradation of GNPs-BSA@TA-Ce and GNPs-BSA separately, in PBS, at 37 °C. The degradation profiles were given in Fig. 4A. No significant difference in cumulative degradation between GNPs-BSA@TA-Ce and GNPs-BSA. Approximately 20 % of GNPs-BSA@TA-Ce had undergone degradation in 7 days. We further examined the biotoxicity of GNPs@TA-Ce and their degradation byproducts on BMDMs using CCK8 assay (Fig. 4B). The results of cell viability tests on 1 day, 3 day and 7 day suggested the by-products and residual undegraded gelatin still exhibited negligible cytotoxicity toward BMDMs. These results indicated that GNPs@TA-Ce showed low cytotoxicity after incubation with BMDMs at the experimental concentration. It made the effective utilization of GNPs-BMP9@TA-Ce *in vitro* and *in vivo* possible.

To further study the effect of GNPs-BMP9@TA-Ce on BMDMs, we labeled GNPs@TA-Ce red fluorescence with RhB, lysosomes green with LysoTracker and nuclei blue with Hoechst. BMDMs were treated with LPS for 6 h to induce inflammatory stimulation. After co-culture with GNPs@TA-Ce for 4 h, a amount of orange staining (the overlap of green and red fluorescence) was observed in the cytoplasm of BMDMs (Fig. 4CI). It demonstrated that GNPs@TA-Ce were mainly endocytosed by BMDMs through the endolysosomal pathway. The pH value in lysosomes is about 5.5–6.5, which can further accelerate the decomposition of TA-Ce and conduct the subsequent responsive release. After incubation for 24 h, rich red fluorescence was observed in the cytoplasm (Fig. 4CII), which suggested that GNPs@TA-Ce escaped from lysosomes successfully in BMDMs because of the proton sponge effect. These confirmed that GNPs@TA-Ce could undergo lysosome-mediated endocytosis in BMDMs and exhibit pH-response within acidic lysosomal compartments.

BMDMs stimulated with LPS (10 ng/mL) were treated with different biomaterial groups. IL-1β were marked by immunofluorescence staining, analyzed by quantitative fluorescence intensity measurement using ImageJ. As shown in Fig. 4D, much higher level of IL-1β after 24 h in the LPS group compared with CON group confirmed the inflammatory microenvironment. In representative images (Fig. 4D), suppression of IL-1β associated red fluorescence was observed in GNPs@TA-Ce and GNPs-BMP9@TA-Ce groups after 24 h co-culture, demonstrating their anti-inflammatory efficacy. Whereas GNPs-BMP9 showed no significant impact. These results suggested that the anti-inflammatory effects on IL-1β was primarily mediated by TA-Ce rather than BMP9. This observation aligned with our previous studies demonstrating the anti-inflammatory capacity of TA-Ce, potentially attributable to the biological activity of Ce [24–26].

3.4. Effect of GNPs-BMP9@TA-Ce on osteoclasts in LPS-induced inflammatory microenvironment

Osteoclasts are well-defined and distinctive in bone marrow, originating from myeloid progenitor or osteal macrophages. Since the origin from monocytes/macrophages were confirmed, more research showed that immature cells of the monocytes/macrophages lineage and mature osteal macrophages can differentiate into osteoclasts. As the important regulatory network in bone metabolism diseases, macrophage-osteoclast axis is attracting increasing research attention [41–44]. Under the stimulation of M-CSF, hematopoietic stem cells in the bone marrow produce monocytes/macrophages lineage, which further differentiate into osteoclasts induced by RANKL. Formation of osteoclastst requires the fusion and multinucleation of macrophages [45]. *In vitro* experiments, BMDMs were induced to undergo osteoclastogenesis by M-CSF and Rankl together. LPS (10 ng/mL) was used to simulate the inflammatory environment. After biomaterials of different groups treatment, we studied the effect of GNPs-BMP9 (0.25 mg/mL)、GNPs-BMP9@TA-Ce (0.25 mg/mL) and GNPs@TA-Ce (0.25 mg/mL) on osteoclasts respectively according to the experimental timeline (Fig. 5A).

3.4.1. Suppression of osteoclasts formation by GNPs-BMP9@TA-Ce

We evaluated the effect of biomaterials on osteoclasts formation with TRAP staining (Fig. 5B). Monocytes/macrophages first commit and become TRAP + mononuclear cells, defined as preosteoclasts; Pre-osteoclasts subsequently fuse to form TRAP + multinuclear cells (TRAP + MNCs), defined as osteoclasts. Cells with fewer nuclei are less mature compared to larger multinuclear cells. In this study, osteoclasts with 3–4 nuclei were defined as more naive, and those with more than 4 nuclei were considered more mature.

According to the number of nuclei in TRAP + MNCs under a light microscope, we quantified the number of osteoclasts in each treatment group.

As shown in Fig. 5B, osteoclastogenesis was induced successfully by 50 ng/mL Rankl in all groups on day 6. It was visually observed the 10 ng/mL LPS group induced more TRAP + MNCs (Fig. 5BII) compared to the control group (without LPS) [Fig. 5BI], suggesting the osteoclasts were activated by the inflammatory microenvironment. Among the treatment groups (all with 10 ng/mL LPS), the quantity of TRAP + MNCs generation and osteoclasts size in the GNPs-BMP9 (Fig. 5BIII) and GNPs-BMP9@TA-Ce (Fig. 5BVI) groups were significantly lower than others. There were more naive osteoclasts. This result demonstrated the inhibitory effect of BMP9 (100 ng/mL) on osteoclasts formation under inflammatory conditions, consistent with another related research [46]; The number of TRAP + MNCs in the GNPs@TA-Ce group was also lower than that in the LPS group and relevant osteoclasts size was significantly smaller, indicating the suppression of TA-Ce on osteoclasts formation. Considering the biocatalytic enzyme properties of TA-Ce under some certain conditions [26], this result may be related to the energy metabolism of osteoclasts. Interestingly, TA-Ce and BMP9 exhibited synergistic inhibitory effects on the osteoclasts formation in an inflammatory microenvironment.

Among the TRAP + cells in the treatment groups, The quantity of preosteoclasts in GNPs-BMP9 and GNPs-BMP9@TA-Ce group remained at a relatively lower level compared to the LPS group, indicating their potential impact on osteoclasts differentiation.

3.4.2. Suppression of osteoclasts function by GNPs-BMP9@TA-Ce

The adhesion between macrophage cells is partially mediated by E-cadherin and integrin, with subsequent cytoskeletal rearrangement. Finally, DCSTAMP mediating membrane fusion, leading to osteoclasts formation through cell-cell fusion [47]. The macrophages close to each other by chemotaxis effect, induced by M-CSF. Fused multinuclear cells are reprogrammed to perform specific functions. The completion of osteoclast differentiation is marked by the expression of mature markers, such as MMP9, TRAP and CTSK [48,49]. The RNA expression of CTSK (Fig. 5CI) was significantly down-regulated after 48 h of treatment in the biomaterial groups, indicating the BMP9 and TA-Ce suppression of its expression collaboratively. CTSK protease decomposes gelatin, elastin, and collagen, playing an important role in the bone repair [50,51]. This revealed GNPs-BMP9 could inhibit the function of mature osteoclasts. The RNA expression of TRAP (Fig. 5CII) was also decreased in GNPs-BMP9, GNPs-BMP9@TA-Ce and GNPs@TA-Ce groups, consistent with the staining result. MMP9 is essential in bone and cartilage repair, regulating osteoclast migration to target tissues [52,53]. The RNA expression of MMP9 (Fig. 5CIII) was significantly down-regulated after 48 h of treatment in the GNPs-BMP9@TA-Ce group.

Consistently, osteoclasts function-associated genes (Trap, MMP9 and CTSK) were significantly down-regulated after 48 h in the GNPs-BMP9@TA-Ce group. These results indicated that osteoclasts function was weakened by the collaborative effect of BMP9 and TA-Ce.

NFATc1 has been demonstrated as an indispensable regulatory factor

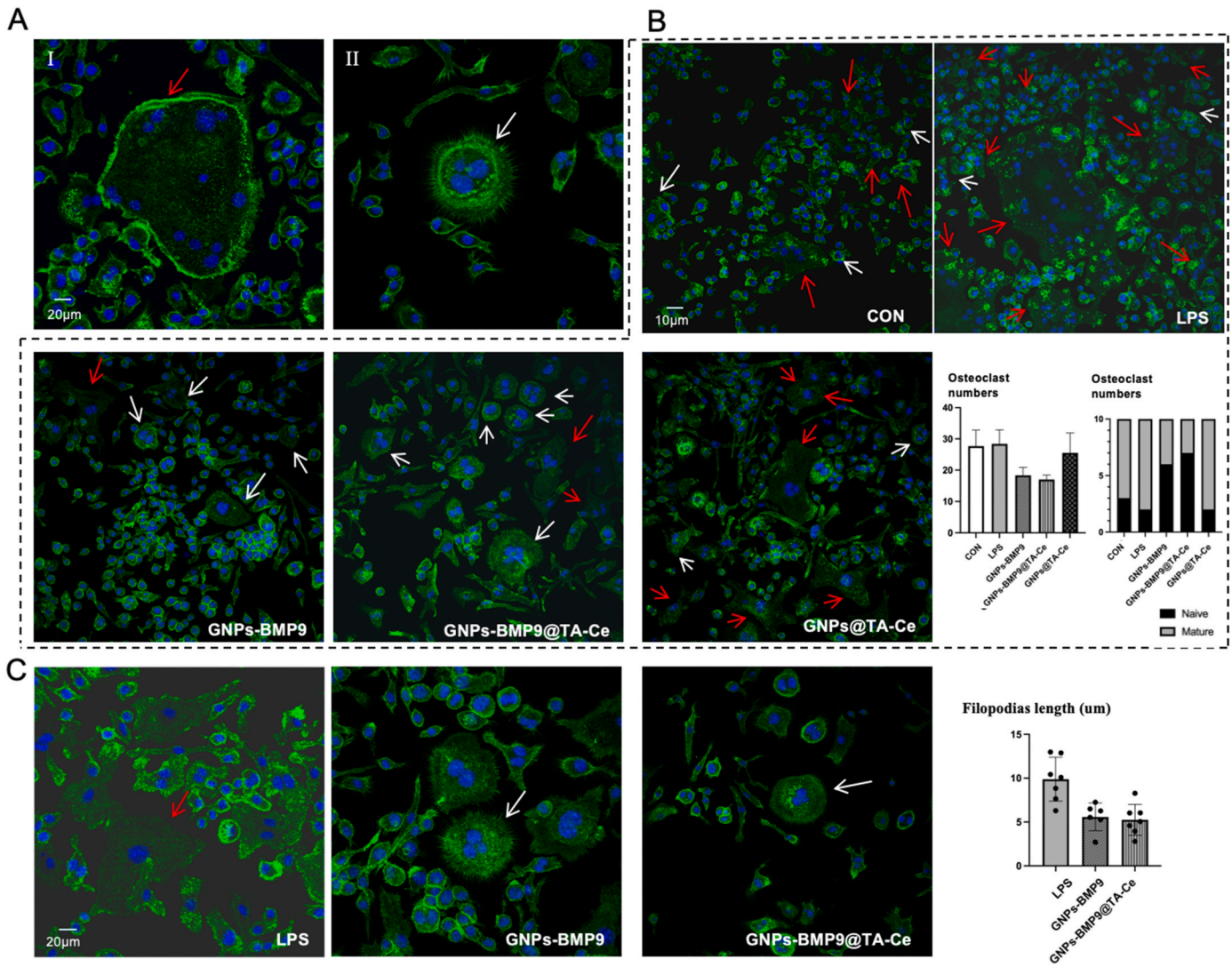

Fig. 6. Effect of GNPs-BMP9@TA-Ce on osteoclasts differentiation **(A)** Representative cytoskeleton staining images of the mature osteoclast with a red arrow (I) and naive osteoclast with a white arrow (II). Scale bar: 20 μm. **(B)** The cytoskeleton staining images of the control, LPS, GNPs-BMP9, GNPs-BMP9@TA-Ce and GNPs@TA-Ce groups and osteoclasts quantitative analysis. Scale bar: 10 μm. **(C)** The differences between the LPS, GNPs-BMP9 and GNPs-BMP9@TA-Ce groups in osteoclasts morphology and quantitative analysis. Scale bar: 20 μm. (For interpretation of the references to color in this figure legend, the reader is referred to the Web version of this article.)

in the pathway of osteoclast formation and differentiation, also playing a significant role in osteoclast activation, fusion, and bone resorption functions [54]. NFATc1 directly regulates the expression levels of target genes by binding to promoter regions, ultimately affecting the formation and functional activity of osteoclasts, such as CTSK, MMP-9, and TRAP [55]. In this study, GNPs-BMP9@TA-Ce inhibited the expression of these osteoclast-related genes. Therefore, the inhibition of osteoclast differentiation by biomaterials was likely to work by downregulating the expression of these related genes and ultimately reducing the expression level of NFATc1. However, the inhibitory effect of GNPs-BMP9@TA-Ce on these osteoclast-related genes was stronger than that on NFATc1 (Fig. 5CIV), and the reason for this phenomenon required further study.

The RNA expression of DC-STAMP gene exhibited no statistically significant differences after 24 h or 48 h in biomaterials treatment groups. This observation may be associated with the degree of osteoclast differentiation studied herein. Cell-cell fusion into multinucleated cells signifies osteoclast differentiation, encompassing the fusion of macrophages with other macrophages, monocytes, and various multinuclear cells. During this process, DC-STAMP typically serves as a fusion marker [56]. Our monitoring of DC-STAMP RNA expression on day 4 and day 5 revealed that these timepoints were not optimal for detecting cell fusion.

3.4.3. *Suppression of osteoclast differentiation by GNPs-BMP9@TA-Ce*

An increased number of nuclei and larger cell size generally indicate more effective products secreted by osteoclasts, reflecting a stronger bone resorption capability [57].

In mature osteoclasts, distinct filopodias and ruffled borders on the actin ring (as in Fig. 6AI) are crucial for adhering to bone tissue and exerting bone resorption, which are important for osteoclasts adhereing to the bone tissue surface and exerting bone resorption. Naive osteoclasts (Fig. 6AII) are characterized by fewer nuclei, a smaller cell size, a more regular shape, and weaker bone resorption function. As shown in Fig. 6B, phalloidin fluorescence staining demonstrated that treatment with GNPs-BMP9@TA-Ce reduced the number of osteoclasts, particularly the larger ones, and decreased the average nuclear count. These findings further corroborate the results of PCR and TRAP staining, suggesting that GNPs-BMP9@TA-Ce can inhibit the formation and function of osteoclasts in an inflammatory microenvironment.

Surprisingly, in the GNPs-BMP9 and GNPs-BMP9@TA-Ce groups, most osteoclasts underwent significant morphological changes:

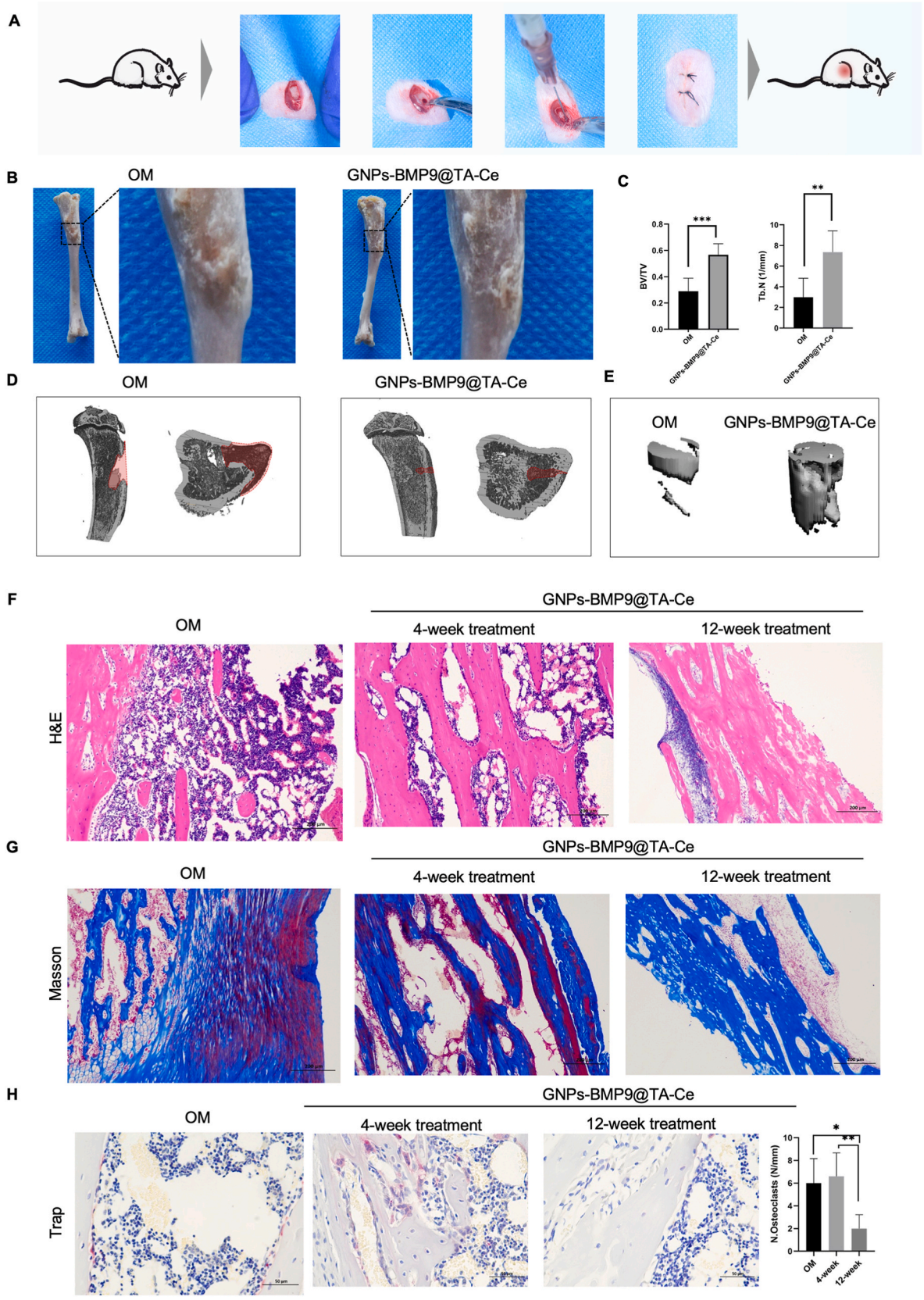

Fig. 7. *In vivo* bone repair effects of GNPs-BMP9@TA-Ce in OM (**A**) Construct an OM model in SD rats. (**B**) Tibia photographs of rats after 4-week treatment. (**C**) The BV/VT and Tb. N analysis after 4-week treatment. (**D**) Micro-CT reconstructed images of tibias after 4-week treatment. (**E**) Micro-CT reconstructed images of defects in tibias after 4-week treatment. (**F**) H&E staining of the tibia tissue after 4-week and 12-week treatment. (**G**) Masson staining of the tibia tissue after 4-week and 12-week treatment. (**H**) Trap staining of the tibia tissue after 4-week and 12-week treatment.

elongated filopodias, disappearance of ruffled borders, thinner and smaller actin rings, decreased cell size, and a more regular, round cell shape (Fig. 6C). These features suggested the presence of more immature osteoclasts, preosteoclasts, and even macrophages. The GNPs@TA-Ce group did not exhibit these characteristics. This result indicated that BMP9 could affect osteoclast maturation, which was rarely reported in previous studies, providing novel insights into the mechanism of BMP9's effect on osteoclasts.

3.5. *In vivo bone repair effect of GNPs-BMP9@TA-Ce*

To assess the *in vivo* effects of GNPs-BMP9@TA-Ce, an OM model of SD rats was constructed to evaluate its therapeutic potential. A defect (diameter 1.5 mm, depth 3 mm) in the tibia was created. S. aureus suspension was injected into the defect to introduce an OM model [58]. One week after the surgery, abnormal bone proliferation can be seen around the defect in Micro-CT images (Fig. S6A). The success of the OM model was further confirmed by an AlamarBlue colorimetric assay of S. aureus from tibial tissue (Fig. S6B). The experimental procedure was outlined in Fig. 7A. To assess *in vivo* effects of GNPs-BMP9@TA-Ce, rats tibias were obtained at 4 weeks and 12 weeks. The images (Fig. 7B) showed better recovery of bone quality on the defect area in the GNPs-BMP9@TA-Ce treatment group. The 4-week treatment of GNPs-BMP9@TA-Ce group achieved more bone repair confirmed by BV/TV quantitative and Tb. N results (Fig. 7C). Micro-CT images demonstrated that the OM group had a larger bone defect area compared to the 4-week treatment group (Fig. 7D). It also showed better bone reconstruction at the site of bone defects (Fig. 7E). These results collectively reflected bone repair effects in an inflammatory microenvironment. Meanwhile, The full blood analysis and liver and kidney function indices of the 4-week treatment group demonstrated the good biocompatibility of GNPs-BMP9@TA-Ce (Figs. S7 and S8). Regulating osteoclast function and differentiation in an inflammatory environment is a major challenge for OM bone repair. To determine whether GNPs-BMP9@TA-Ce modulates bone repair *in vivo*, tibial paraffin sections of rats were analyzed by histological staining. Hematoxylin-eosin (H&E) staining (Fig. 7F) showed extensive infiltration of inflammatory cells, including multinuclear giant cells and neutrophils in the OM group, accompanied by lower bone mass. In the 4-week treatment group, more bone tissue was observed. The 12-week treatment group clearly showed more structured, dense bone tissue. Masson's trichrome staining (Fig. 7G) confirmed significant osteoclast activity and abnormal osteogenesis in the OM group, moderate changes in the 4-week GNPs-BMP9@TA-Ce treatment group, and minimal changes in the 12-week treatment group, aligning with the CT and H&E staining results. Additionally, more new collagen was observed in the 12-week treatment group. Trap staining (Fig. 7H) and osteoclasts number analysis of 4-week and 12-week treatment groups showed more TRAP-positive cells in the 4-week treatment group compared with the OM group, indicating active bone repair in the early stages of chronic inflammation. In later treatment stages, a decrease in osteoclasts was observed, accompanied by bone growth in the treated area. Overall, GNPs-BMP9@TA-Ce effectively modulated bone repair in an inflammatory microenvironment.

In conclusion, GNPs-BMP9@TA-Ce can effectively repair bone defects in OM rats. When injected into the infected bone defect area, GNPs-BMP9@TA-Ce impacte osteoclast biological activity. The acidic and inflammatory microenvironment triggers the release activity of GNPs-BMP9@TA-Ce, enabling responsive sustained release and enhancing drug effects. Degradation of the GNPs-BMP9@TA-Ce shell exposes BMP9, whose properties directly facilitate bone reconstruction. In summary, GNPs-BMP9@TA-Ce successfully promote bone repair in response to an inflammatory microenvironment.

4. Conclusion

Most research on bone defect treatment has focused on extensive antibiotic use and surgery [59,60]. However, promoting bone repair in an inflammatory environment is often overlooked. Given the crucial role of the macrophage-osteoclast axis in the bone-immune system, we synthesized a biomaterial, GNPs-BMP9@TA-Ce, with a "shell-core" structure to exert bone regulation. GNPs-BMP9@TA-Ce integrates the electron-donating effect of TA's multi-hydroxy groups with Ce, forming a classic MPN-Ce network system that achieves pH-responsive release under inflammatory conditions. GNPs@TA-Ce leverages the advantages of GNPs as nanocarriers, capable of loading osteogenic, antibacterial, and anti-inflammatory drugs. We explored the bone repair effect of GNPs-BMP9@TA-Ce in an inflammatory environment using BMP9 as an example and discovered its impact on osteoclast formation, differentiation, and function. It demonstrated sensitivity to pH values, confirming that GNPs-BMP9@TA-Ce can rapidly release adequate drugs and maintain stable drug release at an effective concentration in an inflammatory microenvironment. Consequently, GNPs-BMP9 @TA-Ce successfully achieved bone remodeling in OM rats. In conclusion, GNPs-BMP9@TA-Ce effectively responds to the inflammatory microenvironment, regulating the macrophage-osteoclast axis to achieve bone repair.

CRediT authorship contribution statement

Huan Zeng: Writing – original draft, Methodology, Investigation, Data curation, Conceptualization. **Dize Li:** Writing – original draft, Conceptualization. **Qingqing He:** Methodology, Investigation. **Xinhui Zheng:** Data curation, Conceptualization. **Xu Chen:** Methodology, Investigation. **Guangyu Jian:** Resources, Methodology, Investigation. **Hongmei Zhang:** Writing – review & editing, Funding acquisition, Conceptualization. **Tao Chen:** Writing – review & editing, Supervision, Funding acquisition, Conceptualization.

Funding

This work was supported by the National Outstanding Youth Science Fund Project of National Natural Science Foundation of China (32322044) and the National Natural Science Foundation of China (No. 82470977).

Declaration of competing interest

The authors declare that they have no known competing financial interests or personal relationships that could have appeared to influence the work reported in this paper.

Appendix A. Supplementary data

Supplementary data to this article can be found online at https://doi.org/10.1016/j.mtbio.2025.101777.

Data availability

Data will be made available on request.

References

[1] D.P. Lew, F.A. Waldvogel, Osteomyelitis, Lancet 364 (2004) 369–379, https://doi.org/10.1016/s0140-6736(04)16727-5.
[2] N. Kavanagh, et al., Staphylococcal osteomyelitis: disease progression, treatment challenges, and future directions, Clin. Microbiol. Rev. 31 (2018), https://doi.org/10.1128/cmr.00084-17.
[3] D. Harry, Z. Joseph, Microbiology of acute and chronic osteomyelitis and antibiotic treatment, Dent. Clin. 61 (2017) 271–282, https://doi.org/10.1016/j.cden.2016.12.001.

[4] K.E. Beenken, M.J. Campbell, M.S. Smeltzer, The ability of sarA to limit protease production plays a key role in the pathogenesis of Staphylococcus aureus osteomyelitis irrespective of the functional status of agr, Infect. Immun. (2024) e0047324, https://doi.org/10.1128/iai.00473-24.
[5] J. Olson, et al., Association of antibiotic route and outcomes in children with methicillin-resistant Staphylococcus aureus bacteremic osteomyelitis, Infect. Dis. Ther. (2024), https://doi.org/10.1007/s40121-024-01074-2.
[6] M.J. Campbell, et al., RANKL-mediated osteoclast formation is required for bone loss in a murine model of Staphylococcus aureus osteomyelitis, Bone 187 (2024) 117181, https://doi.org/10.1016/j.bone.2024.117181.
[7] J. Song, et al., Advanced strategies of scaffolds design for bone regeneration, BMEMat 42 (2023) e12046, https://doi.org/10.1002/bmm2.12046.
[8] G. Schett, I.B. McInnes, M.F. Neurath, Reframing immune-mediated inflammatory diseases through signature cytokine hubs, N. Engl. J. Med. 385 (2021) 628–639, https://doi.org/10.1056/NEJMra1909094.
[9] M.Y. Wu, J.H. Lu, Autophagy and macrophage functions: inflammatory response and phagocytosis, Cells 9 (2019), https://doi.org/10.3390/cells9010070.
[10] X. Pan, Q. Zhu, L.L. Pan, J. Sun, Macrophage immunometabolism in inflammatory bowel diseases: from pathogenesis to therapy, Pharmacol. Ther. 238 (2022) 108176, https://doi.org/10.1016/j.pharmthera.2022.108176.
[11] I. Marriott, Apoptosis-associated uncoupling of bone formation and resorption in osteomyelitis, Front. Cell. Infect. Microbiol. 3 (2013) 101, https://doi.org/10.3389/fcimb.2013.00101.
[12] M. Farahani, et al., Enhancing diaphragmatic defect repair and regeneration: how biomaterials leading the way to progress? BMEMat (2024) e12070 https://doi.org/10.1002/bmm2.12070.
[13] M. Hao, et al., Magnetic hydroxyapatite nanobelt-stem cell hybrid spheroids for remotely patterning bone tissues, BMEMat 10 (2023) e12059, https://doi.org/10.1002/bmm2.12059.
[14] C. Wang, et al., Biomaterials for in situ cell therapy, BMEMat 39 (2023) e12039, https://doi.org/10.1002/bmm2.12039.
[15] L. Wang, Y. Yan, A review of pH-responsive organic-inorganic hybrid nanoparticles for RNAi-based therapeutics, Macromol. Biosci. 21 (2021) e2100183, https://doi.org/10.1002/mabi.202100183.
[16] N. Deirram, C. Zhang, S.S. Kermaniyan, A.P.R. Johnston, G.K. Such, pH-responsive polymer nanoparticles for drug delivery, Macromol. Rapid Commun. 40 (2019) e1800917, https://doi.org/10.1002/marc.201800917.
[17] Y. Yan, et al., Nanomedicines reprogram synovial macrophages by scavenging nitric oxide and silencing CA9 in progressive osteoarthritis, Adv. Sci. (Weinh.) 10 (2023) e2207490, https://doi.org/10.1002/advs.202207490.
[18] S.A. Yeh, et al., Quantification of bone marrow interstitial pH and calcium concentration by intravital ratiometric imaging, Nat. Commun. 13 (2022) 393, https://doi.org/10.1038/s41467-022-27973-x.
[19] S.L. Teitelbaum, Bone resorption by osteoclasts, Science 289 (2000) 1504–1508, https://doi.org/10.1126/science.289.5484.1504.
[20] L. Gambari, F. Grassi, L. Roseti, B. Grigolo, G. Desando, Learning from monocyte-macrophage fusion and multinucleation: potential therapeutic targets for osteoporosis and rheumatoid arthritis, Int. J. Mol. Sci. 21 (2020), https://doi.org/10.3390/ijms21176001.
[21] X. Li, et al., Assembly of metal-phenolic/catecholamine networks for synergistically anti-inflammatory, antimicrobial, and anticoagulant coatings, ACS Appl. Mater. Interfaces 10 (2018) 40844–40853, https://doi.org/10.1021/acsami.8b14409.
[22] L. Chen, et al., Metal-phenolic network with Pd nanoparticle nodes synergizes oxidase-like and photothermal properties to eradicate oral polymicrobial biofilm-associated infections, Adv. Mater. 36 (2024) e2306376, https://doi.org/10.1002/adma.202306376.
[23] W. Sang, et al., A triple-kill strategy for tumor eradication reinforced by metal-phenolic network nanopumps, Adv. Funct. Mater. 32 (2022) 2113168, https://doi.org/10.1002/adfm.202113168.
[24] X. Chen, et al., Adaptive nanoparticle-mediated modulation of mitochondrial homeostasis and inflammation to enhance infected bone defect healing, ACS Nano 17 (2023) 22960–22978, https://doi.org/10.1021/acsnano.3c08165.
[25] D. Li, et al., A dual-antioxidative coating on transmucosal component of implant to repair connective tissue barrier for treatment of peri-implantitis, Adv. Healthcare Mater. 12 (2023) e2301733, https://doi.org/10.1002/adhm.202301733.
[26] Q. He, et al., Safeguarding osteointegration in diabetic patients: a potent “chain armor” coating for scavenging ROS and macrophage reprogramming in a microenvironment-responsive manner, Adv. Funct. Mater. 31 (2021) 2101611, https://doi.org/10.1002/adfm.202101611.
[27] Y. Lei, et al., Functional biomaterials for osteoarthritis treatment: from research to application, Smart Med. 16 (2022) e20220014, https://doi.org/10.1002/SMMD.20220014.
[28] S. Young, M. Wong, Y. Tabata, A.G. Mikos, Gelatin as a delivery vehicle for the controlled release of bioactive molecules, J. Contr. Release 109 (2005) 256–274, https://doi.org/10.1016/j.jconrel.2005.09.023.
[29] H. Wang, S.C. Leeuwenburgh, Y. Li, J.A. Jansen, The use of micro- and nanospheres as functional components for bone tissue regeneration, Tissue Eng., Part B 18 (2012) 24–39, https://doi.org/10.1089/ten.TEB.2011.0184.
[30] S.T. Koshy, T.C. Ferrante, S.A. Lewin, D.J. Mooney, Injectable, porous, and cell-responsive gelatin cryogels, Biomaterials 35 (2014) 2477–2487, https://doi.org/10.1016/j.biomaterials.2013.11.044.
[31] K. Dubbin, et al., Macromolecular gelatin properties affect fibrin microarchitecture and tumor spheroid behavior in fibrin-gelatin gels, Biomaterials 250 (2020) 120035, https://doi.org/10.1016/j.biomaterials.2020.120035.
[32] Q. Kang, et al., A comprehensive analysis of the dual roles of BMPs in regulating adipogenic and osteogenic differentiation of mesenchymal progenitor cells, Stem Cell. Dev. 18 (2009) 545–559, https://doi.org/10.1089/scd.2008.0130.
[33] Q. Kang, et al., Characterization of the distinct orthotopic bone-forming activity of 14 BMPs using recombinant adenovirus-mediated gene delivery, Gene Ther. 11 (2004) 1312–1320, https://doi.org/10.1038/sj.gt.3302298.
[34] J. Huang, et al., The role of COX-2 in mediating the effect of PTEN on BMP9 induced osteogenic differentiation in mouse embryonic fibroblasts, Biomaterials 35 (2014) 9649–9659, https://doi.org/10.1016/j.biomaterials.2014.08.016.
[35] H. Zhang, et al., Canonical Wnt signaling acts synergistically on BMP9-induced osteo/odontoblastic differentiation of stem cells of dental apical papilla (SCAPs), Biomaterials 39 (2015) 145–154, https://doi.org/10.1016/j.biomaterials.2014.11.007.
[36] W. Zhang, et al., Inflammatory microenvironment-responsive hydrogels enclosed with quorum sensing inhibitor for treating post-traumatic osteomyelitis, Adv. Sci. (Weinh.) 11 (2024) e2307969, https://doi.org/10.1002/advs.202307969.
[37] M. Sousa de Almeida, et al., Understanding nanoparticle endocytosis to improve targeting strategies in nanomedicine, Chem. Soc. Rev. 50 (2021) 5397–5434, https://doi.org/10.1039/d0cs01127d.
[38] Z.L. Zhang, et al., Systemic Tcell and local macrophage interactions mediategranule size-dependent biological hydroxyapatite foreign body reaction, BMEMat (2023) e12133, https://doi.org/10.1002/bmm2.12133.
[39] H.S. Kwon, M.H. Ryu, C. Carlsten, Ultrafine particles: unique physicochemical properties relevant to health and disease, Exp. Mol. Med. 52 (2020) 318–328, https://doi.org/10.1038/s12276-020-0405-1.
[40] Y.R. Xu, et al., Electrospun fiber-based immune engineering in regenerative medicine, Smart Medicine 12 (2024) e2023003, https://doi.org/10.1002/SMMD.20230034.
[41] H. Takayanagi, RANKL as the master regulator of osteoclast differentiation, J. Bone Miner. Metabol. 39 (2021) 13–18, https://doi.org/10.1007/s00774-020-01191-1.
[42] N. Udagawa, et al., Origin of osteoclasts: mature monocytes and macrophages are capable of differentiating into osteoclasts under a suitable microenvironment prepared by bone marrow-derived stromal cells, Proc. Natl. Acad. Sci. USA 87 (1990) 7260–7264, https://doi.org/10.1073/pnas.87.18.7260.
[43] L. Li, et al., Calf thymus polypeptide improved hematopoiesis via regulating colony-stimulating factors in BALB/c mice with hematopoietic dysfunction, Int. J. Biol. Macromol. 156 (2020) 204–216, https://doi.org/10.1016/j.ijbiomac.2020.03.041.
[44] C. Baeck, et al., Pharmacological inhibition of the chemokine C-C motif chemokine ligand 2 (monocyte chemoattractant protein 1) accelerates liver fibrosis regression by suppressing Ly-6C(+) macrophage infiltration in mice, Hepatology 59 (2014) 1060–1072, https://doi.org/10.1002/hep.26783.
[45] P. Hernigou, et al., Osteonecrosis repair with bone marrow cell therapies: state of the clinical art, Bone 70 (2015) 102–109, https://doi.org/10.1016/j.bone.2014.04.034.
[46] Y.M. Zhou, et al., BMP9 reduces bone loss in ovariectomized mice by dual regulation of bone remodeling, J. Bone Miner. Res. 35 (2020) 978–993, https://doi.org/10.1002/jbmr.3957.
[47] Y. Yao, et al., The macrophage-osteoclast Axis in osteoimmunity and osteo-related diseases, Front. Immunol. 12 (2021) 664871, https://doi.org/10.3389/fimmu.2021.664871.
[48] K.H. Park-Min, Metabolic reprogramming in osteoclasts, Semin. Immunopathol. 41 (2019) 565–572, https://doi.org/10.1007/s00281-019-00757-0.
[49] T. Sugatani, et al., Ligand trap of the activin receptor type IIA inhibits osteoclast stimulation of bone remodeling in diabetic mice with chronic kidney disease, Kidney Int. 91 (2017) 86–95, https://doi.org/10.1016/j.kint.2016.07.039.
[50] L.H. Gao, S.S. Li, H. Yue, Z.L. Zhang, Associations of serum cathepsin K and polymorphisms in CTSK gene with bone mineral density and bone metabolism markers in postmenopausal Chinese women, Front. Endocrinol. 11 (2020) 48, https://doi.org/10.3389/fendo.2020.00048.
[51] X. Lin, et al., Smart nanosacrificial layer on the bone surface prevents osteoporosis through acid-base neutralization regulated biocascade effects, J. Am. Chem. Soc. 142 (2020) 17543–17556, https://doi.org/10.1021/jacs.0c07309.
[52] D. Egorov, I. Kopaliani, A.K. Ameln, S. Speier, A. Deussen, Mechanism of pro-MMP9 activation in co-culture of pro-inflammatory macrophages and cardiomyocytes, Exp. Cell Res. 434 (2024) 113868, https://doi.org/10.1016/j.yexcr.2023.113868.
[53] C. Xue, et al., Aconine attenuates osteoclast-mediated bone resorption and ferroptosis to improve osteoporosis via inhibiting NF-κB signaling, Front. Endocrinol. 14 (2023) 1234563, https://doi.org/10.3389/fendo.2023.1234563.
[54] C. Fang, et al., Diterbutyl phthalate attenuates osteoarthritis in ACLT mice via suppressing ERK/c-fos/NFATc1 pathway, and subsequently inhibiting subchondral osteoclast fusion, Acta Pharmacol. Sin. 43 (2022) 1299–1310, https://doi.org/10.1038/s41401-021-00747-9.
[55] Z. Zhong, et al., NFATc1-mediated expression of SLC7A11 drives sensitivity to TXNRD1 inhibitors in osteoclast precursors, Redox Biol. 63 (2023) 102711, https://doi.org/10.1016/j.redox.2023.102711.
[56] W. Wisitrasameewong, et al., DC-STAMP is an osteoclast fusogen engaged in periodontal bone resorption, J. Dent. Res. 96 (2017) 685–693, https://doi.org/10.1177/0022034517690490.
[57] Q. Xiang, et al., Beyond resorption: osteoclasts as drivers of bone formation, Cell Regen. 13 (2024) 22, https://doi.org/10.1186/s13619-024-00205-x.

[58] J. Min, et al., Designer dual therapy nanolayered implant coatings eradicate biofilms and accelerate bone tissue repair, ACS Nano 10 (2016) 4441–4450, https://doi.org/10.1021/acsnano.6b00087.
[59] J.W. Choi, et al., Asian facial recontouring surgery, Plast Aesthet Res 10 (2023) 59, https://doi.org/10.20517/2347-9264.2023.30.
[60] L. Autelitano, M.C. Meazzini, Alveolar cleft reconstruction with vomerine bone: two surgical procedures in one step: a case series, Plast Aesthet Res 10 (2023) 16, https://doi.org/10.20517/2347-9264.2022.57.